Research Square

Preprints are preliminary reports that have not undergone peer review.
They should not be considered conclusive, used to inform clinical practice,
or referenced by the media as validated information.

Direct amplification of octave-spanning coherent infrared spectra enabled by chirped quasi-phase matching

Yuxin Leng

lengyuxin@mail.siom.ac.cn

Shanghai Institute of Optics and fine mechanics, Chinese Academy of Sciences
https://orcid.org/0000-0002-2716-4318

Renyu Feng
Shanghai Institute of Optics and Fine Mechanics

Junyu Qian
Shanghai Institute of Optics and Fine Mechanics

Yanyan Li
Shanghai Institute of Optics and Fine Mechanic Chinese Academy of Sciences

Wenkai Li
Shanghai Institute of Optics and Fine Mechanic Chinese Academy of Sciences

Tianshun Sun
Shanghai Institute of Optics and fine mechanics

Yinuo Guo
Shanghai Institute of Optics and fine mechanics

Yujie Peng
Shanghai Institute of Optics and Fine Mechanics

Ruxin Li
Shanghai Institute of Optics and Fine Mechanics

Article

Keywords:

Posted Date: November 27th, 2026

DOI: https://doi.org/10.21203/rs.3.rs-11756946/v1

License: This work is licensed under a Creative Commons Attribution 4.0 International License.
Read Full License

Additional Declarations: There is **NO** Competing Interest.

Direct amplification of octave-spanning coherent infrared spectra enabled by chirped quasi-phase matching

Renyu Feng,[1] Junyu Qian,[1,✉] Yanyan Li,[1] Wenkai Li,[1] Tianshun Sun,[1,2] Yinuo Guo,[1,2] Yujie Peng,[1,2,✉] Yuxin Leng,[1,2,✉] and Ruxin Li[1]

[1] State Key Laboratory of Ultra-intense Laser Science and Technology, Shanghai Institute of Optics and Fine Mechanics, Chinese Academy of Sciences, Shanghai 201800, China
[2] School of Physics and Optoelectronic Engineering, Hangzhou Institute for Advanced Study, University of Chinese Academy of Sciences, Hangzhou 310024, China
✉ qianjunyu@siom.ac.cn; yjpeng@siom.ac.cn; lengyuxin@mail.siom.ac.cn

Abstract Broadband coherent laser sources spanning optical octaves are essential for advancing ultrafast spectroscopy, waveform synthesis, and attosecond science. However, direct amplification of octave-spanning spectra remains a fundamental challenge because the finite phase-matching bandwidth of nonlinear crystals prevents conventional optical parametric amplification (OPA) from simultaneously providing efficient gain over an ultrabroadband spectral range. Here, we introduce chirped quasi-phase matching (CQPM) for direct amplification of octave-spanning coherent spectra. By engineering the nonlinear reciprocal lattice through a tailored chirped polarization structure, different spectral components satisfy their optimal phase-matching conditions at different positions inside a single nonlinear crystal, enabling distributed spectral amplification. Using a dispersion-poling co-designed chirped periodically poled lithium niobate crystal in a two-stage OPA, we demonstrate broadband parametric amplification covering signal and idler spectra from 1.3 to 4.2 μm with a pulse energy of 65 μJ at 1 kHz repetition rate. The CEP-stabilized mid-infrared idler pulses support a transform-limited duration approaching a single optical cycle.

Understanding and controlling the microscopic dynamics of matter requires light sources capable of simultaneously providing ultrahigh temporal resolution, broad spectral coverage, and precise phase coherence. The motions of electrons[1,2], atoms[3], and molecules[4,5] occur on femtosecond[6] to attosecond[7] timescales, driving fundamental processes ranging from chemical reactions and energy transport to quantum dynamics. Consequently, ultrashort laser pulses have become indispensable tools for probing and manipulating matter through techniques such as ultrafast spectroscopy, pump–probe measurements, and high-field light–matter interactions. However, accessing these ultrafast phenomena often requires laser sources with increasingly broader spectral bandwidths. In particular, octave-spanning coherent pulses can further support the generation of single-cycle optical waveforms[1], enabling applications including frequency-comb spectroscopy, waveform synthesis, and isolated attosecond pulse generation[8].

Mid-infrared (MIR) is the fingerprint region of molecular vibrations, combined with ultrafast femtosecond lasers, broadband MIR sources enable direct observation of molecular vibrations, chemical bond dynamics, and collective excitations in condensed matter. To date, broadband MIR femtosecond pulses have become indispensable tools for ultrafast absorption spectroscopy, with applications in probing crystal lattice dynamics, atmospheric remote sensing, molecular and cellular fingerprinting[9,10], and related fields[11,12]. In particular, MIR supercontinuum covering the entire spectral region enable simultaneous multi-component

measurements within a single laser shot[13,14], significantly improving both the speed and accuracy of spectroscopic analysis. Beyond spectroscopy, broadband MIR pulses are also emerging as powerful drivers for high-field physics[8,15]. The generation of isolated attosecond pulses[7] through high-order harmonic generation (HHG)[16,17] relies on few-cycle driving pulses[18,19] with octave-spanning spectra. Extending the driving wavelength into the MIR region further enhances the harmonic cutoff energy due to the ponderomotive potential related to the laser wavelength, providing a promising route toward high-energy attosecond photon sources[16]. Therefore, a high-quality, CEP-stable MIR supercontinuum seed is crucial for isolated attosecond pulse driving lasers.

Due to the limited emission bandwidth of conventional MIR laser gain media, it is nearly impossible to directly generate octave-spanning MIR supercontinuum pulses through stimulated emission alone. Frequency-conversion techniques, particularly optical parametric amplification (OPA) based on second-order nonlinear interactions, provide an effective approach for broadband pulse generation across a wide spectral range[20,21]. However, although OPA can support relatively broad gain bandwidths, the large phase mismatch associated with octave-spanning spectra prevents nonlinear crystals from providing efficient gain over the entire spectral region simultaneously. Therefore, the most widely adopted approach for generating supercontinuum pulses relies on secondary spectral broadening through self-phase modulation (SPM)[1,22-24]. Although this approach has enabled remarkable advances in broadband pulse generation, it intrinsically separates energy amplification and spectral broadening into independent processes. The spectral broadening stage inevitably introduces energy loss and additional higher-order spectral phase, complicating pulse compression and waveform control. Moreover, because SPM strongly depends on the driving intensity, fluctuations in the input pulse energy can directly translate into spectral instability. These limitations become particularly significant for applications requiring highly stable, phase-controlled broadband MIR sources. Therefore, a method capable of directly amplifying octave-spanning coherent spectra remains a fundamental challenge in ultrafast photonics.

To achieve direct amplification of MIR supercontinuum lasers, the nonlinear crystal must provide an ultrabroad gain bandwidth capable of covering the entire supercontinuum spectrum. At present, several approaches have been developed to overcome the bandwidth limitation of conventional OPA. Frequency-domain optical parametric amplification[25] (FOPA) increases the effective gain bandwidth by spatially separating different spectral components in a Fourier plane and employing nonlinear crystals with different phase-matching conditions. Dual-chirped optical parametric amplification[26,27] (DCOPA) utilizes broadband pump and signal pulses with tailored chirp profiles, allowing different pump and signal wavelength pairs to satisfy the phase-matching condition at a single crystal angle, thereby achieving ultrabroadband amplification. Although these approaches have successfully extended the achievable amplification bandwidth, they rely on complex optical architectures or stringent requirements on pump and seed pulse engineering. More importantly, a broadband seed source must be generated before these amplification process. Thus, they do not fundamentally address the challenge of directly amplifying a supercontinuum spectrum within a compact nonlinear interaction.

Quasi-phase matching (QPM) is a technique that introduces a periodic polarization (or domain-inverted) structure into a nonlinear medium, utilizing its reciprocal lattice vector to compensate for phase mismatch caused by dispersion[28,29]. Unlike birefringence-based phase-matching methods, QPM does not rely on the intrinsic birefringent properties of the crystal.

Instead, flexible control of nonlinear interactions can be achieved simply by designing appropriate periodic domain structures[30,31]. Therefore, we introduce chirped quasi-phase matching (CQPM) method. In contrast to conventional OPA, where all spectral components compete for a limited phase-matching bandwidth, CQPM engineers a specially designed domain structure with a chirped varying poling period inside the crystal. Different frequency components satisfy their optimal phase-matching conditions at different positions inside a single nonlinear crystal, transforming uniform spectral amplification into distributed spectral amplification. This unique phase-matching architecture provides an unprecedented route toward direct amplification of octave-spanning coherent spectra.

In this work, we introduce a direct amplification method of octave-spanning coherent spectra enabled by CQPM. Through rigorous dispersion control engineering and polarization-matching design, based on a two-stage OPA amplifier, broadband signal and idler pulses covering across the 1.3 μm to 4.2 μm wavelength range with an output power of 65 mW was simultaneous achieved. In particular, the CEP-stabilized MIR idler pulses can support a single cycle duration. This femtosecond laser source, characterized by its ultra-broad bandwidth, ultra-fast time scale, and CEP stability, not only provides the technical foundation for research in pump-probe nonlinear spectroscopy but also serves as an excellent seed source for the construction of attosecond scientific facilities.

Gain bandwidth of CQPM

In conventional OPA, efficient energy transfer requires the momentum conservation condition between the pump, signal, and idler waves,

$$\Delta k = k_p - k_s - k_i = 0 \quad (1)$$

to be satisfied within the nonlinear interaction length. Although birefringent phase matching or QPM can compensate phase mismatch at a selected wavelength, the corresponding crystal orientation or nonlinear grating remains essentially fixed along the propagation direction. Consequently, different spectral components experience different phase mismatches and only a limited spectral region can obtain efficient gain, resulting in an intrinsic bandwidth limitation for broadband amplification.

This limitation can be overcome by allowing the phase-matching condition itself to evolve spatially, so that each spectral component is amplified near the axial position at which it is locally phase-matched. CQPM provides a direct realization of this concept by engineering the nonlinear reciprocal lattice along the crystal propagation direction. According to distributed spectral amplification, CQPM-OPA transforms the conventional picture of uniform spectral amplification into a spatially engineered nonlinear interaction, where the gain bandwidth is determined not by a single phase-matching condition but by a varying phase-matching landscape. Accordingly, by engineering the polarization period lengths to produce longitudinally evolving phase-matching profiles for distinct spectral bands along the crystal axis and to enable spatially segmented spectral amplification at discrete axial positions, we demonstrate ultra-broadband amplification across the 1.3-4.2 μm spectral band in a 10-mm-long CPPLN crystal.

Structurally, CQPM crystals primarily induce chirped periodic variations in the second-order nonlinear coefficient by incorporating a nonlinear superlattice structure, resulting in a position-dependent quasi-phase-matching condition. This modulation enables the generation of additional reciprocal lattice vectors $\frac{2\pi}{\Lambda_n(z)}$ during nonlinear frequency conversion to

compensate for phase mismatch. As shown in Fig. 1**a**, $\Lambda_n(z)$ is the length of different polarization periods. Based on the phase matching in the different spectral regions,

$$\Delta k_{\text{eff}}(z) = k_p - k_s - k_i - \frac{2\pi}{\Lambda_n(z)} \quad (2)$$

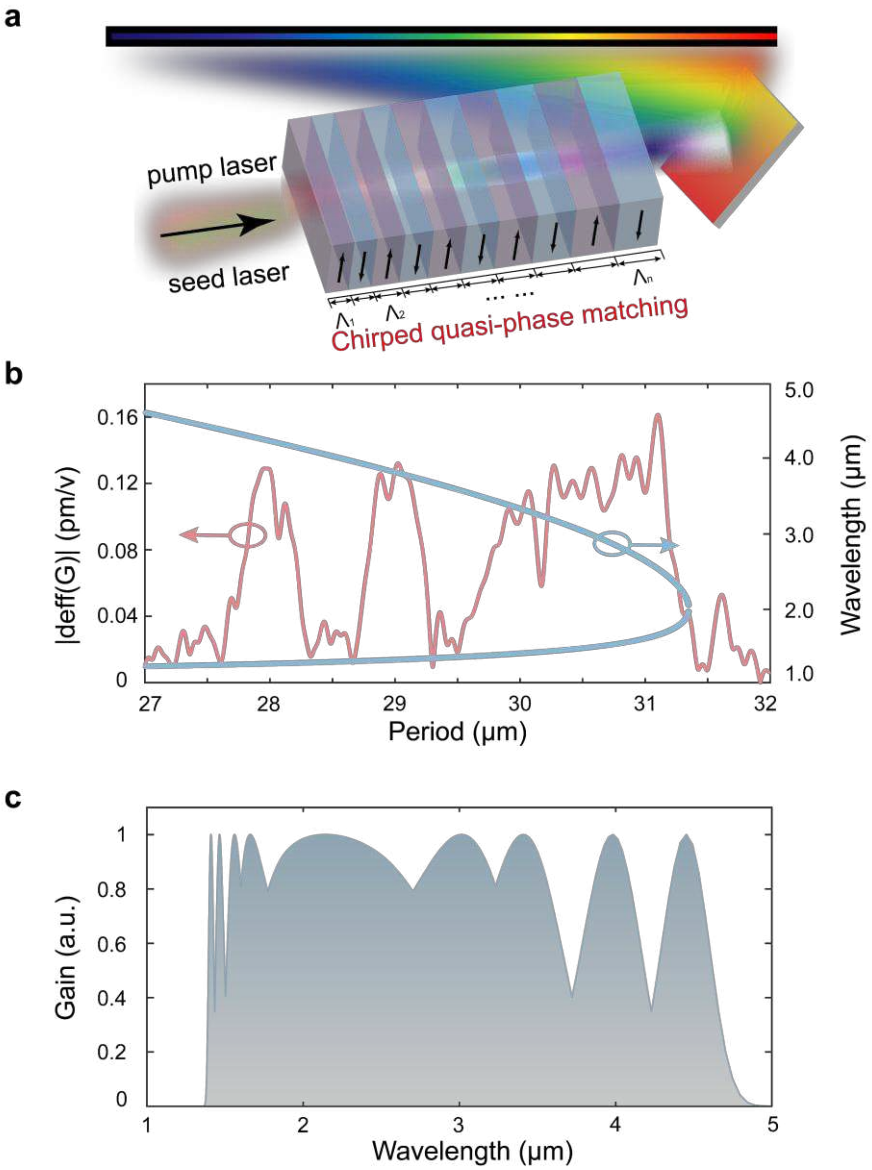

Fig. 1 Structural feature and gain bandwidth of CQPM. a, Structural diagram of CQPM. **b**, Calculated distributions of the effective nonlinear coefficient as functions of the periods for the CPPLN sample, phase-mismatch curves for parametric down conversion as functions of the period for the CPPLN sample. **c**, Normalized gain curves of the OPA process across different spectral components.

The polarization period required to compensate for the phase mismatch can be calculated. In our system, the spectral range of the signal pulse is 1.3-2 μm, and that of the pump pulse is 1.02-1.04 μm. The corresponding λ–Λ relation for a conventional PPLN crystal is shown as the blue curve in Fig. 1**b**. Notably, this relation is markedly nonlinear rather than linear in λs, this feature that turns out to be important for the design. Because the λ(Λ) dispersion is

intrinsically nonlinear, a linear chirp cannot deliver uniform gain, which means the spatial distribution of polarization periods must be matched to the actual local sensitivity $d\lambda/d\Lambda$ of the crystal, not to a constant chirp rate. This nonlinearity has a direct consequence: a linearly chirped period (constant $d\Lambda/dz$) implicitly assigns a disproportionately long interaction length to short-wavelength components, for which $d\lambda/d\Lambda$ is small, while progressively compressing the effective interaction length available to longer-wavelength components. The resulting gain is therefore strongly wavelength-dependent, the short-wavelength edge will be enhanced and the long-wavelength edge will be suppressed, degrading overall spectral flatness. Uniform, distributed spectral amplification thus cannot be achieved with a simple linear chirp; instead, the spatial distribution of the reciprocal lattice must be matched to the actual, nonlinear $\lambda(\Lambda)$ dispersion of the crystal.

Guided by this principle, we designed the polarization-period distribution according to two criteria: sufficient parametric gain at every wavelength, and continuous, seamless coverage of the target band. Only when both are satisfied can distinct spectral components be efficiently amplified at their respective optimal axial positions. From the $\lambda(\Lambda)$ curve in Fig. 1**b**, phase matching across 1.3-4.2 μm requires polarization periods spanning 28-31.5 μm. Within this range, the local sensitivity $d\lambda/d\Lambda$ varies markedly across the spectrum, it describes how strongly the phase-matched wavelength responds to a change in period. Over 1.6-3.2 μm, $d\lambda/d\Lambda$ is large, so this entire range can be covered by just two discrete periods, 30.5 and 31 μm. Accordingly, the period interval is kept shorter to ensure a sufficient interaction length for each wavelength component. In contrast, $d\lambda/d\Lambda$ decreases sharply toward both the 1.3-1.6 μm and 3.2-4.2 μm edges, phase matching becomes far less sensitive to Λ and a larger number of discrete periods is required to preserve seamless coverage. The interaction length available for each wavelength component becomes longer than before, so a longer interval between poling periods can be adopted. By evaluating the phase-matching bandwidth associated with each candidate period (Supplementary Information), we find that three additional periods (28, 29 and 30 μm) are sufficient to extend seamless coverage across these two edge regions.

Combining these five discrete polarization periods (28, 29, 30, 30.5 and 31 μm) arranged sequentially along the crystal axis, we achieve continuous, spatially segmented phase matching spanning the entire 1.3-4.2 μm band (Fig. 1**b**). The robustness of this segmented design is corroborated by the effective Fourier spectral amplitude $d_{eff}(\Lambda)$, which quantifies the nonlinear coupling strength associated with each reciprocal-lattice component under a given phase mismatch Δk. Across the full 28-31.5 μm working range, $d_{eff}(\Lambda)$ exceeds 0.12 pm/V, partially compensating for the shorter interaction length available to the edge segments and helping to preserve gain uniformity across the entire design.

Finally, we calculated the normalized parametric gain spectrum for each 2-mm-long poling segment (five segments, 2 mm×5 = 10 mm total crystal length; Fig. 1**c**). The five gain profiles overlap continuously across their respective phase-matching bands, yielding seamless coverage from 1.3 to 4.2 μm with comparatively uniform gain across this ultra-broadband mid-infrared range and validating the CQPM as an effective route to ultrabroadband parametric amplification.

Supercontinuum laser based on CQPM-OPA

Fig. 2**c** presents the total spectra measured after the two-stage CQPM-OPA, exhibiting a remarkably flat spectral profile spanning 1.3-4.2 μm at -50 dB (1.35-4.1 μm at -25 dB), with

a total energy of 65 μJ across the amplified 1.3-4.2 μm band. This spectrum originates from coherent superposition of the signal and idler pulses via the unique phase-matching mechanism of CQPM. The balanced intensity distribution reflects the delicate interplay between nonlinear phase-matching process across different frequency ranges. Based on precise dispersion control, this ensures highly efficient parametric amplification across different wavelength regions simultaneously, excessive consumption in any single process would compromise the spectral flatness. Furthermore, the corresponding idler spectrum after the second stage (Fig. 2**e**) spans 2 to 4.2 μm, together covering the full target range without any spectral discontinuities. As shown in Fig. 2**d**, there is a certain degree of difference for the spectra of two-stage OPA signal pulses. The moderate difference between the signal spectra of the two amplification stages originates from the distinct polarization period sequences of the quasi-phase-matched crystals employed in each stage.

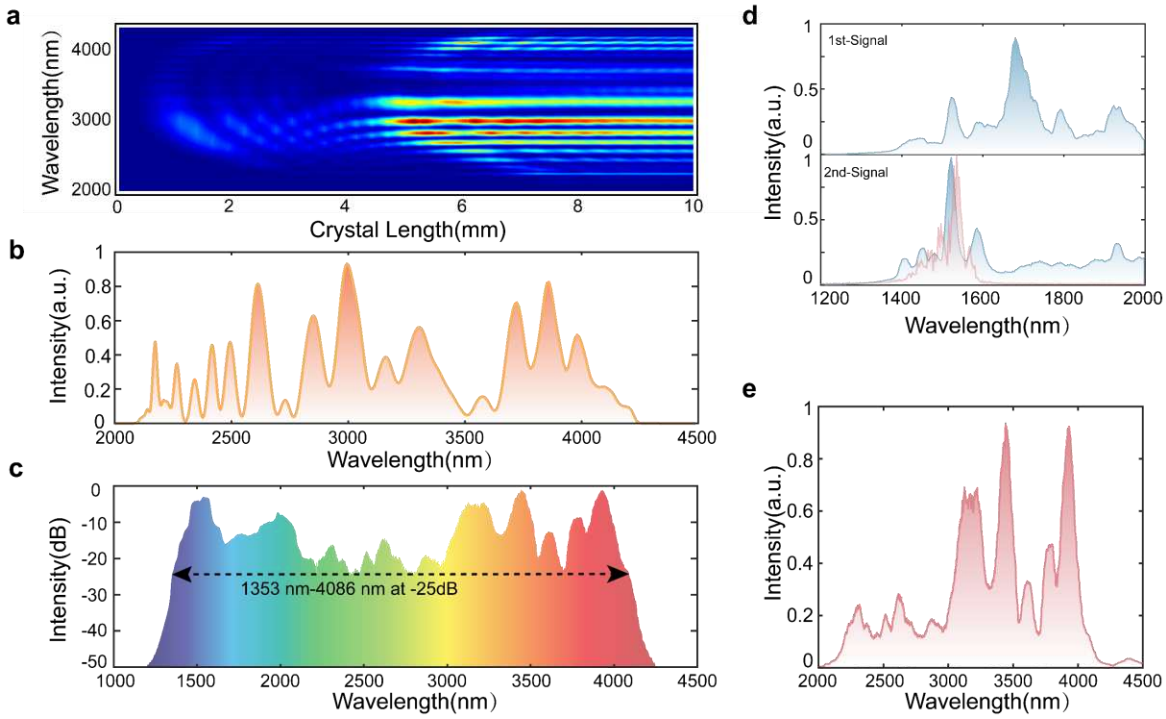

Fig. 2 Visualization of spectral propagation within a CPPLN nonlinear crystal and spectral analysis of two-octave infrared laser. a Simulated spectral evolution of the idler pulses within a 10 mm CPPLN crystal. **b** Simulated output spectra of the idler pulses. **c** Spectra of the amplified supercontinuum. **d** Spectra of the signal pulses (Blue curves are based on the nonlinear chirped CPPLNs, and the red curve is based on the linear chirped CPPLN). **e** Spectra of the idler pulses.

The CQPM-OPA enables parametric amplification over multiple spectral bands spanning several octaves by tailoring the quasi-phase-matching condition along the crystal. Different polarization periods provide phase matching for different spectral regions, enabling the direct amplification of an ultrabroadband coherent spectrum. To achieve both an ultrabroad gain bandwidth and a spectrally flat gain profile, two CPPLN crystals with opposite chirp orientations are employed in a cascaded two-stage OPA. In the first stage, the polarization period decreases along the propagation direction, whereas in the second stage the chirp direction is reversed, with the shorter periods located at the crystal entrance. This

complementary configuration compensates for the wavelength-dependent gain imbalance introduced by a single chirped crystal and significantly improves the gain uniformity across the entire amplification bandwidth. For comparison, the parametric amplification performance of the linearly-chirped periodically-poled lithium-niobate (CPPLN) crystal is also characterized. The red curve in Fig. 2**d** also shows the signal laser spectrum after the two-stage OPA. As we can see, due to the nonlinearity inherent to phase-matching, rigorous spatiotemporal coupling for phase-matching over different spectral bands cannot be achieved via linear chirping. At a fixed nonlinear interaction length, amplification is realized only for selected wavelengths, whereas other spectral bands receive no amplification as a result of temporal walk-off and phase mismatch.

However, Although the chirped QPM design ensures phase matching across the full bandwidth (as discussed above), the experimentally observed continuous and gap-free amplification further demonstrates that each spectral component maintains temporal overlap with the pump at its respective phase-matching position. A condition that is not automatically satisfied in broadband chirped interactions subject to group velocity mismatch (GVM).

To explain this process more clearly, we established a CQPM-OPA model using the split-step Fourier method (SSFM), and calculated the time-domain and frequency-domain evolution of each OPA stage by theoretically solving the optical parametric model of the three-wave mixing equations. We solve the three-wave coupling equations of the CQPM process in cylindrical coordinates. This numerical analysis provides a detailed explanation of how the unique structure of the CPPLN coordinates multiple nonlinear processes to achieve an ultra-broadband spectrum while maintaining good phase-matching efficiency across different spectral regions. The detailed calculation procedures are provided in Supplementary Information Section 2. Fig. 2**a** shows the simulated spectral evolution of the idler pulses at second stage OPA. In contrast to the first-stage amplifier, the CPPLN crystal in the second stage has the short period at the front and the long period at the back. During the initial stage of nonlinear interaction, due to the fact that the idler pulses after the first-stage amplification have relatively low energy in the 3.1 - 4.2 μm wavelength range, small-signal amplification of idler pulses in the 3.1-4.2 μm range is achieved in the 0–2 mm region of the crystal due to phase matching of the long-wavelength component occurring first. Subsequently, with the introduction of the long-cycle, the amplification of the long-wavelength portion of the idler pulse weakened, and the short-wavelength portion (2–3.1 μm) began to achieve precise phase matching. At a distance of 8–10 mm from the crystal, the full-spectrum parametric amplification of the idler pulse reaches saturation, achieving high gain.

This sequential, wavelength-ordered amplification originates from the intrinsic chirp of the supercontinuum-generated signal seed. The wavelength-to-time mapping imparted during supercontinuum generation, via self-phase modulation and material dispersion, naturally aligns with the spatial evolution of the local phase-matching wavelength along the chirped grating. Consequently, each spectral component reaches its phase-matching position precisely as it temporally overlaps with the pump pulse, enabling seamless energy transfer across the entire bandwidth in the absence of additional dispersion compensation. The numerically simulated idler spectrum is presented in Fig. 2**b**, featuring a flat and uniform profile across the full bandwidth. It is in excellent agreement with the experimental measurement shown in Fig. 2**e**. This consistency validates the alignment between our theoretical framework and experimental observations. By engineering the crystal's quasi-phase-matching properties and applying precise spatiotemporal coupling and dispersion management, we establish a perfect mapping of wavelength, time, and phase-matching

period along the spatial evolution. Therefore, through theoretical numerical calculations and experimental verification, it has been demonstrated that precise dispersion control and phase-matching design can effectively achieve infrared pulse amplification across octaves while ensuring high conversion efficiency.

Under the OPA architecture, ultra-wideband amplification was achieved across 1.7 octaves in the 1.3–4.2 μm range based on the synergistic nonlinear effects of multi-period phase matching. As shown in Fig. 3**a** and **b**, the calculated Fourier-transform limitation (FTL) pulse widths of the signal and idler pulses are 12.2 fs and 11 fs respectively (2.2 optical cycles at 1.65 μm and 1.06 optical cycle at 3.1 μm). Admittedly, complex higher-order dispersion effects may arise during parametric amplification across multiple frequency ranges. However, such higher-order dispersion can be precisely compensated for using programmable acousto-optic modulators, thereby providing the technical foundation for realizing milliwatt-level single-cycle mid-infrared light sources.

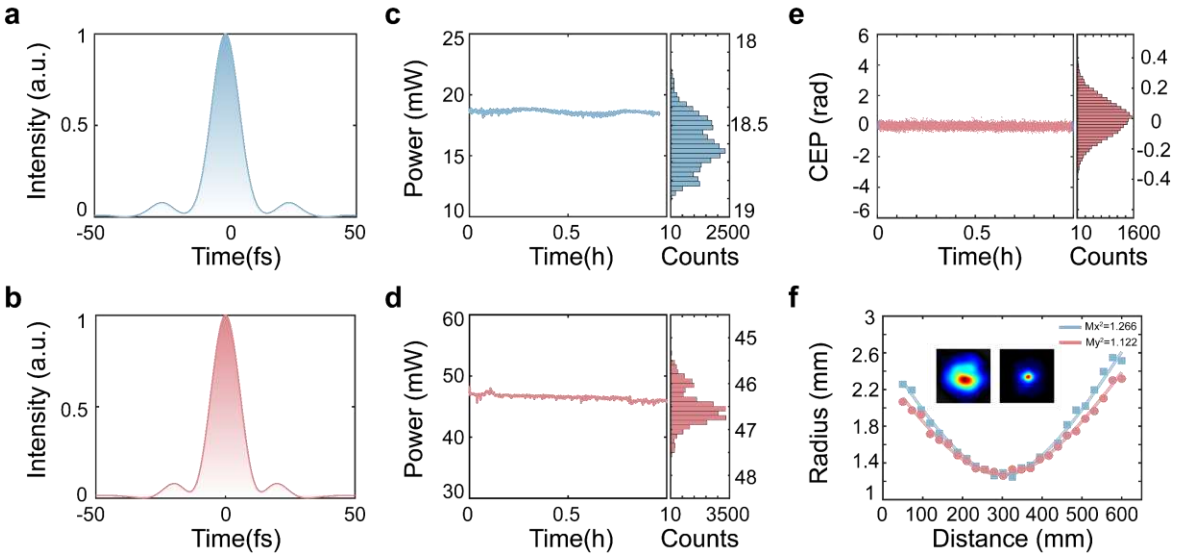

Fig. 3 Calculated FTL pulse shapes of the supercontinuum and measurements of the single-shot CEP in the f-to-2f interferometer and Power stability. a and **b** Calculated FTL pulse shapes of the signal and idler pulses. **c** Power stability of the output idler pulses, the RMS error of the power is evaluated to 0.47% for one hour. **d** Power stability of the output signal pulses, the RMS error of the power is evaluated to 0.9% for one hour. **e** The RMS error of the CEP shift is evaluated to be 125 mrad for one hour. **f** Evolution of the beam diameters (full width at e^2 maximum) along the x axis (horizontal direction, blue circles) and y axis (vertical direction, red squares) with the beam propagation across the focal point.

In the experiment, we use a stable laser source as the driving laser. During supercontinuum generation, a variable density filter and an iris diaphragm control the energy to produce a stable supercontinuum to give the OPA system a stable seed light. By using a stable seed light and optimizing the spatial and temporal coupling during amplification, we can improve the stability of the entire system as much as possible. To characterize the long-term operational stability of the OPA system, we evaluate both the carrier-envelope phase (CEP) stability and pulse energy stability. As presented in Fig. 3**c** and 3**d**, the root-mean-square (RMS) energy fluctuation is measured to be 0.9% for 46.5 μJ signal pulses and 0.47% for 18.5 μJ idler pulses.

Based on the $E_i(\omega_i) \propto E_p(\omega_p)E_s^*(\omega_s), \quad \phi_i = \phi_p - \phi_s$, the signal and idler pulses are coherently generated, with their phases governed by the pump phase. Because the idler field is the phase conjugate of the signal, its carrier-envelope phase is intrinsically and passively locked, without requiring any active stabilization loop. An f-to-2f interferometer[20] is implemented to characterize the CEP stability of the MIR idler pulses. The CEP values are demonstrated in Fig. 3**e** with an RMS value of 125 mrad for one hour. This exceptionally stable CEP is achieved through precise control of nonlinear effects during the experiment, which avoids high-intensity nonlinear perturbations and enables ultra-stable passive phase locking.

Meanwhile, the quality of the focus beam profile is one of the great concerns in the ultrafast science experiments. The measure diameter evolutions of the focusing beam profile up to two times the Rayleigh length across the focal point are recorded in the horizontal (Fig. 3**f**, blue squares) and vertical (Fig. 3**f**, red circles) directions, respectively. The obtained M^2 values (defined at the central wavelength of 3.1 μm) of the focus beam profile were 1.26 and 1.12 in the horizontal and vertical directions, respectively.

Conclusions

The CPPLN crystals are used to realize distributed spectral amplification for ultra-wideband parametric down-conversion, where deliberate dispersion management is jointly engineered with the chirped poling period to achieve QPM over an ultra-wide bandwidth. Based on this precise and simple dispersion management and poling-period design, by employing two-stage OPA amplification, laser generation across the 1.3 to 4.2 μm wavelength range with an output power of 65 mW was achieved at a repetition rate of 1 kHz. In particular, the spectral range of CEP-stabilized MIR idler pulse spans over an octave, the FTL reaches a single cycle.

This dispersion-poling co-design strategy of CQPM is general and can be extended to even broader bandwidths, offering a new paradigm for designing next-generation, highly integrated ultra-broadband and even single-cycle light sources. With a future ultra-broadband Dazzler covering this full bandwidth, such a source could in principle be directly compressed into the single-cycle, high-power regime. This femtosecond light source, characterized by its ultra-broad bandwidth, ultrafast time scale, and CEP stability, not only provides the technical foundation for pump-probe nonlinear spectroscopy but also serves as an excellent seed source for the construction of attosecond large-scale scientific facilities. In addition, in conjunction with rapidly advancing research in lithium niobate micro- and nanomaterials, it is also expected that highly integrated on-chip ultra-broadband supercontinuum laser sources will be realized.

References

1 Zorin, I., Gattinger, P., Ebner, A. & Brandstetter, M. Advances in mid-infrared spectroscopy enabled by supercontinuum laser sources. *Optics express* **30**, 5222-5254 (2022).

2 Dantus, M., Rosker, M. J. & Zewail, A. H. Real-time femtosecond probing of ‘‘transition states’’ in chemical reactions. *The Journal of Chemical Physics* **87**, 2395-2397, doi:10.1063/1.453122 (1987).

3 Schiffrin, A. *et al.* Optical-field-induced current in dielectrics. *Nature* **493**, 70-74, doi:10.1038/nature11567 (2013).

4 Higuchi, T., Heide, C., Ullmann, K., Weber, H. B. & Hommelhoff, P. Light-field-driven currents in graphene. *Nature* **550**, 224-228, doi:10.1038/nature23900 (2017).
5 Megerle, U., Pugliesi, I., Schriever, C., Sailer, C. F. & Riedle, E. Sub-50 fs broadband absorption spectroscopy with tunable excitation: putting the analysis of ultrafast molecular dynamics on solid ground. *Applied Physics B* **96**, 215-231 (2009).
6 Zewail, A. H. Laser Femtochemistry. *Science* **242**, 1645-1653, doi:10.1126/science.242.4886.1645 (1988).
7 Geneaux, R. *et al.* Synthesis and characterization of attosecond light vortices in the extreme ultraviolet. *NATURE COMMUNICATIONS* **7**, doi:10.1038/ncomms12583 (2016).
8 Uiberacker, M. *et al.* Attosecond real-time observation of electron tunnelling in atoms. *Nature* **446**, 627-632, doi:10.1038/nature05648 (2007).
9 Camp Jr, C. H. *et al.* High-speed coherent Raman fingerprint imaging of biological tissues. *Nature photonics* **8**, 627-634 (2014).
10 Camp Jr, C. H. & Cicerone, M. T. Chemically sensitive bioimaging with coherent Raman scattering. *Nature photonics* **9**, 295-305 (2015).
11 Schriever, C., Lochbrunner, S., Riedle, E. & Nesbitt, D. J. Ultrasensitive ultraviolet-visible 20fs absorption spectroscopy of low vapor pressure molecules in the gas phase. *Review of Scientific Instruments* **79**, 013107, doi:10.1063/1.2834877 (2008).
12 Tkachenko, N. V. in *Optical Spectroscopy* 61-87 (Elsevier Science, 2006).
13 Hannaford, P. *Femtosecond laser spectroscopy*. (Springer Science & Business Media, 2004).
14 Liebel, M., Toninelli, C. & van Hulst, N. F. Room-temperature ultrafast nonlinear spectroscopy of a single molecule. *Nature Photonics* **12**, 45-49 (2018).
15 Payeur, S. *et al.* Generation of a beam of fast electrons by tightly focusing a radially polarized ultrashort laser pulse. *Applied Physics Letters* **101**, 041105, doi:10.1063/1.4738998 (2012).
16 Popmintchev, T. *et al.* Bright Coherent Ultrahigh Harmonics in the keV X-ray Regime from Mid-Infrared Femtosecond Lasers. *Science* **336**, 1287-1291, doi:10.1126/science.1218497 (2012).
17 Ishii, N. *et al.* Carrier-envelope phase-dependent high harmonic generation in the water window using few-cycle infrared pulses. *Nature Communications* **5**, 3331, doi:10.1038/ncomms4331 (2014).
18 Qian, J. *et al.* Pulse combination and compression in hollow-core fiber for few-cycle intense mid-infrared laser generation. *Photonics Research* **9**, 477-483 (2021).
19 Feng, R. *et al.* TW-scale few-cycle short-wave infrared laser based on nonlinear compression in a large-core gas-filled hollow core fiber. *Applied Physics Letters* **125** (2024).
20 Wang, P. *et al.* 2.6 mJ/100 Hz CEP-stable near-single-cycle 4 μm laser based on OPCPA and hollow-core fiber compression. *Optics Letters* **43**, 2197-2200 (2018).
21 Beutler, M. *et al.* Difference-frequency generation of ultrashort pulses in the mid-IR using Yb-fiber pump systems and AgGaSe2. *Optics Express* **23**, 2730-2736 (2015).
22 Jiang, X. *et al.* Deep-ultraviolet to mid-infrared supercontinuum generated in solid-core ZBLAN photonic crystal fibre. *Nature Photonics* **9**, 133-139 (2015).
23 Elu, U. *et al.* Seven-octave high-brightness and carrier-envelope-phase-stable light source. *Nature Photonics* **15**, 277-280 (2021).

24 Dudley, J. M., Genty, G. & Coen, S. Supercontinuum generation in photonic crystal fiber. *Reviews of modern physics* **78**, 1135-1184 (2006).
25 Gruson, V. *et al.* 2.5 TW, two-cycle IR laser pulses via frequency domain optical parametric amplification. *OPTICS EXPRESS* **25**, 27706-27714, doi:10.1364/OE.25.027706 (2017).
26 Xu, L. *et al.* 100-mJ class, sub-two-cycle, carrier-envelope phase-stable dual-chirped optical parametric amplification. *OPTICS LETTERS* **47**, 3371-3374, doi:10.1364/OL.455811 (2022).
27 Xu, L. & Takahashi, E. J. Dual-chirped optical parametric amplification of high-energy single-cycle laser pulses. *NATURE PHOTONICS* **18**, doi:10.1038/s41566-023-01331-9 (2024).
28 Hong, L. *et al.* Intense ultraviolet–visible–infrared full-spectrum laser. *Light: Science & Applications* **12**, 199 (2023).
29 Hong, L. *et al.* mJ-level 7-octave ultraflat white laser encompassing 200–25,000 nm. *Light: Science & Applications* **15**, 72 (2026).
30 Wu, T. H. *et al.* Visible-to-ultraviolet frequency comb generation in lithium niobate nanophotonic waveguides. *NATURE PHOTONICS* **18**, 218-223, doi:10.1038/s41566-023-01364-0 (2024).
31 Jankowski, M. *et al.* Ultrabroadband nonlinear optics in nanophotonic periodically poled lithium niobate waveguides. *OPTICA* **7**, 40-46, doi:10.1364/OPTICA.7.000040 (2020).

Methods

Experimental details

For broadband parametric amplification, a 5×2×10 mm^3 CPPLN crystal was employed. The crystal consisted of five QPM sections with polarization periods of 28, 29, 30, 30.5, and 31 μm, respectively, and each section had an interaction length of 2 mm. Extended Data Fig. 1**b** show the calculated QPM diagram and the corresponding gain characteristics over different wavelength regions. We engineer the crystal's quasi-phase-matching properties and implement precise spatiotemporal coupling and dispersion management. This approach establishes a perfect mapping of wavelength, time, and phase-matching period throughout the spatial evolution. the phase mismatch among different spectral components can be effectively compensated. Within this framework, phase matching and temporal coupling are simultaneously achieved across a bandwidth exceeding one octave.

Extended Data Fig. 1**a** shows the experimental setup of the octave-spanning OPA system. The driving source was a Yb:YAG laser delivering 400 μJ pulses at 1030 nm with a pulse duration of 900 fs (full width at half maximum, FWHM) and a beam diameter of 1.4 mm. The octave-spanning OPA system consisted of two components: (i) a white-light continuum (WLC) generator and (ii) a cascaded two-stage optical parametric amplifier. The 400 μJ, 1030 nm pump pulse is divided into three beams using two beam splitters (R/T = 80:20). After BS2, a microjoule-level pulse was focused into a 15-mm-thick yttrium aluminum garnet (YAG) crystal through a lens (f=50 mm), generating a broadband supercontinuum extending beyond 2.1 μm via self-phase modulation (SPM). The incident pulse energy is optimized using an aperture and tunable attenuators to achieve stable supercontinuum generation, providing a broadband seed source for subsequent parametric amplification. The spectral component from 1.3 to 2.0 μm is selected as the signal pulse for the first-stage OPA.

In the first amplification stage, the pump beam is collimated to a diameter of 0.7 mm and spatially and temporally overlapped with the supercontinuum seed inside the CPPLN crystal. After efficient parametric amplification, the amplified signal pulse is recollimated using a lens (L, f = 50 mm). Subsequently, the remaining 320 μJ pump pulse reflected by BS1 was combined with the amplified signal and injected into the second collinear OPA stage. After the second-stage amplification, the residual pump beam is removed using DM4. The pump intensities in the first and second OPA stages are 16.6 GW/cm^2 and 20.7 GW/cm^2, respectively. Finally, the CQPM-OPA delivers direct amplification of a 1.7-octave (1.3–4.2 μm) coherent spectrum, with a total output pulse energy of 65 μJ and an idler energy of 18.5 μJ.

Acknowledgements This work was funded by the National Key R&D Program of China (2023YFA1608504); the National Natural Science Foundation of China (22227901, 62305353, 62505333); Talent Plan of Shanghai Branch, Chinese Academy of Sciences; the CAS Project for Young Scientists in Basic Research (YSBR-115).

Author contributions

J.Q., Y.P. and Y.L. conceived and supervised the research. R.F. and J.Q. designed and performed the experiment. R.F. conducted the simulations. R.F., J.Q, Y.L., W.L, T.S and Y.G. interpreted the data. All authors contributed to the preparation of the paper.

Competing interests The authors declare no competing interests.

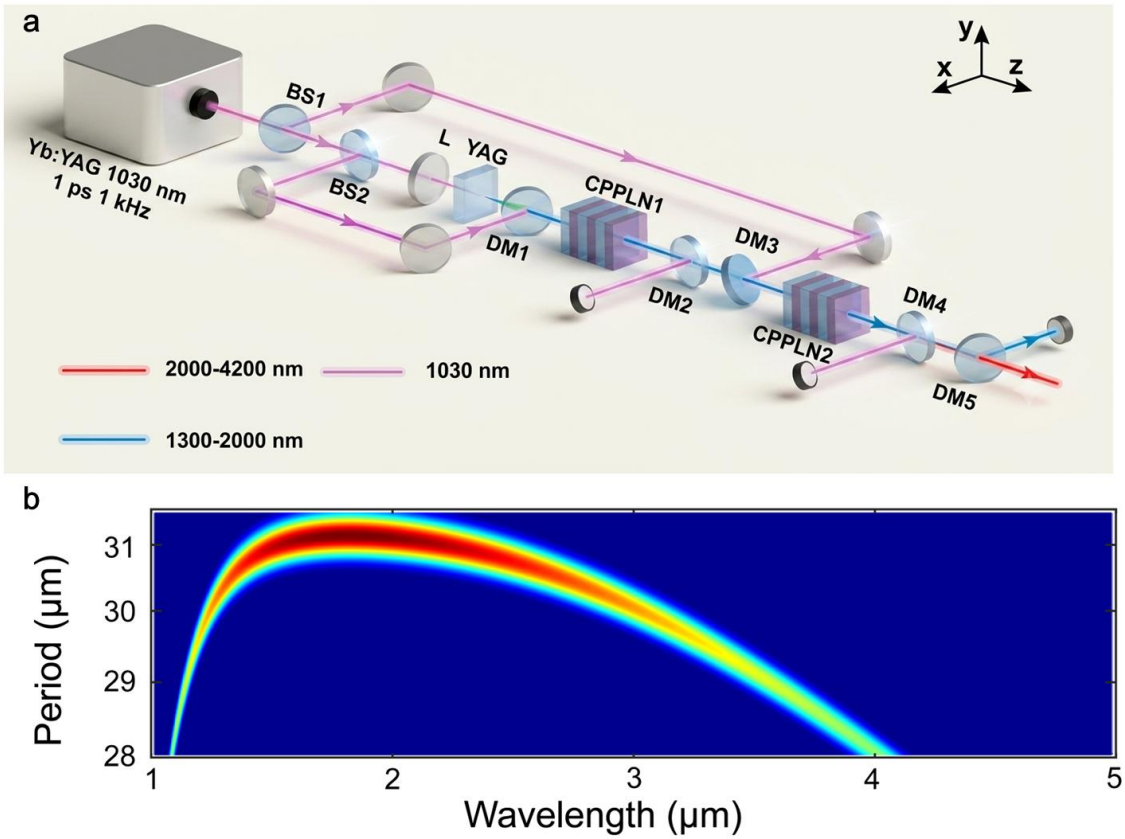

Extended Data Fig. 1 Schematic of the experimental setup and simulated quasi phase-matching curve. a Schematic of the experimental setup. BS, beam splitter; L, lens; YAG, yttrium aluminum garnet crystal; DM, dichroic mirror; CPPLN, chirped periodically poled lithium niobate crystal. **b** Simulated quasi phase-matching curve of the QPA process.

Supplementary information

Amplification of over-octave mid-infrared supercontinuum pulses based on chirped quasi-phase matching

Section 1: QPM analysis of CPPLN.

At this section, we make a detailed qualitative quasi-phase matching (QPM) analysis on chirped-PPLN (CPPLN) sample to evaluate the performance of OPA. To achieve efficient ultrabroad parametric amplification, the most important condition is the successful compensation of specific wave-vector mismatch Δk_i by the appropriate (reciprocal lattice vectors) RLV bands of CPPLN. For a second-order nonlinear process, the slow-varying equation for the amplitude of its second harmonic process can be expressed as

$$\frac{dE_3}{dz} = i\omega\left(\frac{E_1 E_2}{n_2 c}\right)\chi^{(2)}(z)\exp(-i\Delta kz) \tag{S1}$$

To ensure energy transfer between the pump pulse, idler pulse, and signal pulse, the key lies in eliminating the phase-matching factor $\exp(-i\Delta kz)$. Under quasi-phase-matched conditions, the phase mismatch Δk can be directly compensated for by adjusting the nonlinear polarizability tensor factors $\chi^{(2)}(z)$.

Expand the Fourier series of the $\chi^{(2)}(z)$ -factor: $\chi^{(2)}(z) = \sum_{i=-\infty}^{+\infty}\chi_i \exp\left(i\frac{2\pi}{\Lambda_i}z\right)$. Therefore, the mentioned slow-varying equation for the amplitude further developed to :

$$\frac{dE_3}{dz} = \sum_{i=-\infty}^{+\infty}\chi_i\, i\omega\left(\frac{E_1 E_2}{n_2 c}\right)\exp\left(i\left(\frac{2\pi}{\Lambda_i} - \Delta k\right)z\right) \tag{S2}$$

As shown in Fig. S1**a**, for phase mismatches Δk at different wavelengths, quasi-phase matching can be achieved by adjusting the RLV $\frac{2\pi}{\Lambda_i}$ of the CPPLN crystal, allowing energy to be continuously transferred from the pump light field to the signal and idler light fields.

Therefore, to achieve continuous phase matching across an ultra-broad spectral range, we employ a chirped periodically poled lithium niobate (CPPLN) structure, in which the local poling period $\Lambda(z)$ varies continuously along the propagation direction z rather than remaining constant. Physically, each sufficiently short local segment within the crystal, with a length small enough to be treated as possessing a locally uniform period, acts as an independent quasi-phase-matching (QPM) unit that enables phase matching for a narrow spectral band centered at the wavelength dictated by its local period. As the interacting fields propagate through the crystal, they sequentially traverse regions with distinct local periods, each of which delivers efficient parametric gain for a distinct portion of the spectrum. Consequently, the overall device bandwidth is no longer governed by the (narrow) acceptance bandwidth of a single period, but instead by the union of all locally phase-matched spectral bands spanned by the chirp.

In the experiment, the key design is that how to use several periods and how densely to space them. In terms of spectral coverage, the wavelength of pump laser covers 1.02-1.04 μm, in order to achieve the parametric conversion of 1.3-4.2 μm, we calculated the phase-matching curves corresponding to different polarization periods, as shown in the Fig. S1**c-g**. The white curves are the spectra of pump laser, and the area where it overlaps with the phase-matching curve represents the phase matching that can be achieved under this polarization period. According to Fig.S1**c**, the curve for the 28 μm period could provide enough gain to

the signal pulses and idler pulses that cover 1.35-1.42 μm, 4.2-4.6 μm. In the Fig. S1**d-g**, the curves for the 29 μm, 30 μm, 30.5 μm and 31 μm are also effectively for compensation the idler pulses and signal pulses at 4.1- 4.3 μm, 1.41-1.43 μm, 3.7-4.2 μm, 1.42-1.51 μm, 3.0-3.8 μm, 1.5-1.63 μm and 1.6-3.2 μm. Therefore, by introducing reciprocal lattice vectors with different periods, full-band phase matching can be achieved in the 1.3-4.2 μm range.

In terms of nonlinear coupling strength, as clearly plotted in Fig. 1**a**, with 2 mm interaction, 28 μm-31 μm band with the largest Fourier coefficient (χ_{eff}~0.12 pm/v) can successfully provides a good possibility to realize efficient second nonlinear process through a complete coverage of the wave-vector mismatching Δki against a wide signal range from 1.3-4.2 μm. Obviously, by controlling different polarization periods and selecting the nonlinear interaction length, parametric amplification in the 1.3-4.2 μm range can be effectively achieved simultaneously. Furthermore, these highly optimized CPPLN crystals show great promise for creating infrared lasers with higher pulse energy, higher peak power, wider bandwidth, and greater spectral flatness.

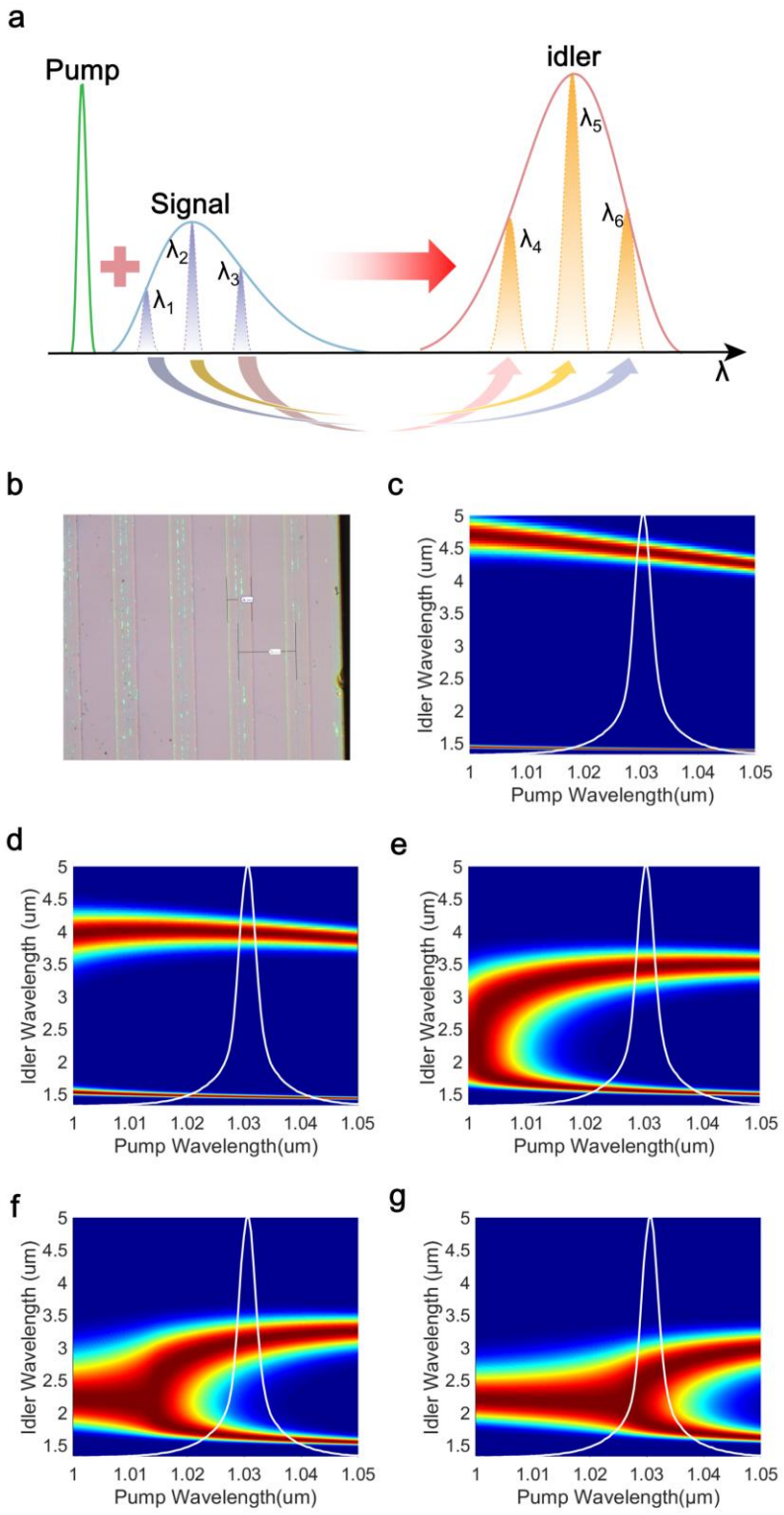

Fig S1. Phase-matching curves for different polarization periods. a Schematic diagram of parametric down-conversion based on CQPM. **b** Microstructure image of the surface of a chirped structure lithium niobate

crystal. c-g CQPM curves based on polarization periods of 28, 29, 30, 30.5, and 31 μm.

Section 2: Analysis of the Phase-Matched Parametric Amplification Process.

In a chirped-PPLN crystal, the polarization period Λ(z) varies continuously with the propagation coordinate z. The spatial dependence has a direct temporal consequence because the GVM between the pump, signal and idler pulses is wavelength-dependent. In other words, the phase-matching condition and temporal walk-off evolve simultaneously along the propagation direction z, rather than constituting independent processes. As the three interacting waves propagate through the crystal, the locally phase-matched wavelength at each position must coincide with the wavelength at which temporal overlap is maintained between the pump, signal and idler pulses. CQPM does not require the introduction of o light and e light components to compensate for GVD, so the signal light, idler light, and pump light undergo parametric amplification in the same polarization state. According to its refractive index Sellmeier's equations, phase matching condition can be satisfied, and the most efficient conversion is obtained in the z plane. This eliminates the spatial walk-off angle intrinsic to birefringent schemes and leaves GVM as the only source of temporal walk-off to be managed.

We calculate the phase mismatch condition pumped with Yb:YAG laser centered at 1030 nm, and the calculated GVM curves for QPM of CPPLN crystal under 1030 nm pump. For the signal in the wavelength range of 1.3-4.2 μm, we can find that the maximum value of GVM is less than 120 fs/mm. In other words, for a 1 ps pump pulse, the time delay between the pump and signal pulses is within ±480 fs at a nonlinear interaction length of 10 mm. At the center wavelength of 3 μm for the idler pulse, the time delay between the pump, signal and idler pulses is within 60 fs/mm. This ensures that, throughout the nonlinear process, the pump, signal and idler pulses overlap temporally across most of their spectral regions. The local walk-off is small enough to sustain efficient energy transfer. At the same time, as shown by the GVD in Fig. S2**b**, the pulse's temporal width remains essentially unchanged throughout the OPA process.

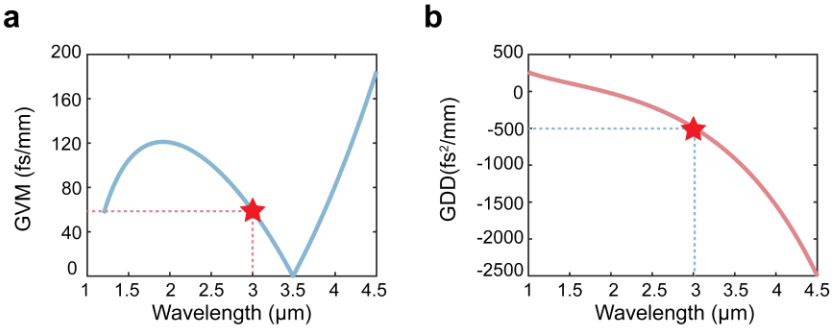

Fig. S2 Evolution curves of GVM and GDD for laser pulses as a function of wavelength. **a** Pump – signal group velocity mismatch curves for CPPLN OPA at the pump wavelength of 1030 nm. **b** The group velocity dispersion curves of CPPLN.

Under precise dispersion control, we designed broadband phase matching by adjusting the polarization period and solved the three-wave coupling equations for chirped quasi-phase matching in a cylindrical coordinate reference frame using the Split-Step Fourier method (SSFM). Since the time scales of the pump pulses, signal pulses, and idle pulses are on the

sub-ps order of magnitude, a slow-varying envelope approximation is applied to the electric fields of these three frequency components:

$$E_j(r,t,z) = Re\left[A_j(r,t,z)exp\left(ik_{j0}z - i\omega_{j0}t\right)\right], \quad j \in \{p,s,i\} \tag{S3}$$

In the simulated architecture, the polarization periods are 28, 29, 30, 30.5, 31 μm, respectively, and the nonlinear effective range for each polarization period is 2 mm. In the defined cylindrical coordinate system, the slow-varying envelope approximation of the three-wave coupling equations is given by:

$$\frac{\partial A_p}{\partial z} = \frac{i}{2k_{p0}}\nabla_\perp^2 A_p - i\sum_{n\geq 2}\frac{\rho_n^{(p)}}{n!}\left(i\frac{\partial}{\partial t}\right)^n A_p - \frac{1}{v_{g,p}}\frac{\partial A_p}{\partial t} + i\kappa_p A_s A_i^* e^{-i\phi(z)} \tag{S4}$$

$$\frac{\partial A_\mathrm{s}}{\partial z} = \frac{i}{2k_{\mathrm{s}0}}\nabla_\perp^2 A_\mathrm{s} - i\sum_{n\geq 2}\frac{\rho_n^{(\mathrm{s})}}{n!}\left(i\frac{\partial}{\partial t}\right)^n A_\mathrm{s} - \frac{1}{v_{g,s}}\frac{\partial A_\mathrm{s}}{\partial t} + i\kappa_p A_\mathrm{i} A_p^* e^{+i\phi(z)}$$

$$\frac{\partial A_\mathrm{i}}{\partial z} = \frac{i}{2k_{\mathrm{i}0}}\nabla_\perp^2 A_\mathrm{i} - i\sum_{n\geq 2}\frac{\rho_n^{(\mathrm{i})}}{n!}\left(i\frac{\partial}{\partial t}\right)^n A_\mathrm{i} - \frac{1}{v_{g,i}}\frac{\partial A_\mathrm{i}}{\partial t} + i\kappa_p A_\mathrm{p} A_\mathrm{s}^* e^{+i\phi(z)}$$

Among them, the nonlinear coupling coefficient is $\kappa_j = \frac{d_{\mathrm{eff}}\,\omega_{j0}}{n_{j0}\,c}$, The accumulation of phase due to partial phase mismatch can be expressed as $\triangle k_0(z) = k_{p0} - k_{s0} - k_{i0} - K_g(z)$. We simplify the linear propagation term into a linear operator and modify the three-wave coupling equations for chirped quasi-phase-matched coupling described above.

$$\frac{\partial A_\mathrm{p}}{\partial z} = L_\mathrm{p}A_\mathrm{p} + i\kappa_s A_\mathrm{s} A_i^* e^{-i\phi(z)} \tag{S5}$$

$$\frac{\partial A_s}{\partial z} = L_s A_s + i\kappa_s A_\mathrm{i} A_p^* e^{+i\phi(z)}$$

$$\frac{\partial A_\mathrm{i}}{\partial z} = L_\mathrm{i}A_\mathrm{i} + i\kappa_s A_\mathrm{p} A_\mathrm{s}^* e^{+i\phi(z)}$$

We use single-step SSFM to calculate these equations, $A_j(z + \triangle z) = \widehat{L_J^{(1/2)}}\widehat{N_J}(\triangle z)\widehat{L_J^{(1/2)}}A_j(z)$. Nonlinear phase evolution is calculated using symmetric SSFM, and the wavenumber relationships in the angular spectrum domain are controlled through precise spatiotemporal algorithms.

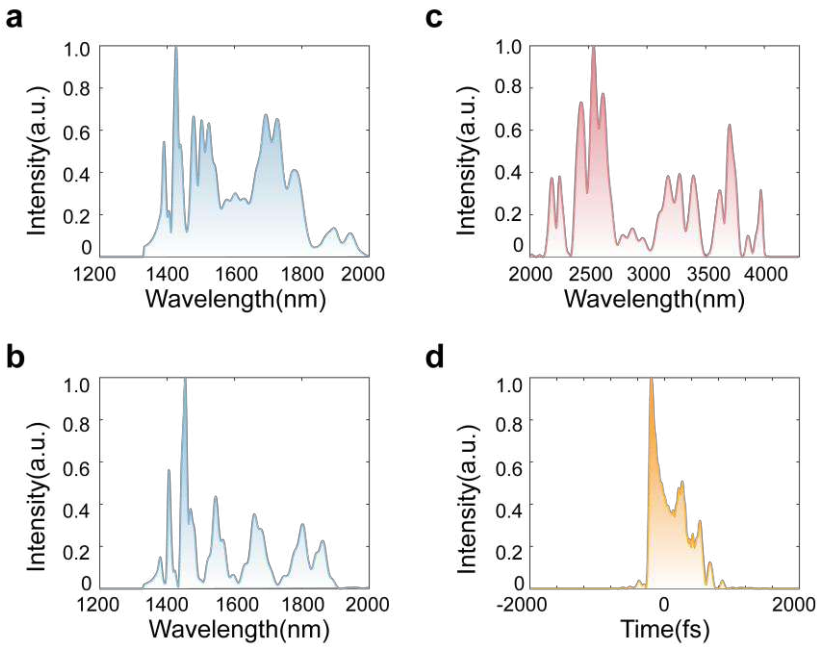

Fig. S3 Simulated spectral and domain characteristics of CQPA. Simulated output spectra of the **a** first-stage CQPA signal pulses and **b** second-stage CQPA signal pulses. **c** **S**imulated output spectra of the first-stage CQPA idler pulses. **d** Simulated pulse envelope of the output idler pulses.

Under the aforementioned architecture, we simulated and calculated the two-stage OPA process. By optimizing the speed of group velocity walk-off and phase matching, we are able to achieve multi-spectral-band parametric conversion simultaneously. As shown in Fig. S3, the output spectra of the signal and idler pulses at each stage are in good agreement with the experimental results. The signal pulses amplified by the first-stage OPA are stronger in the long-wavelength region, primarily because the long polarization period occurs first, allowing it to take priority in utilizing the stronger pump pulses. In the second stage, the gain in the short-wavelength region is compensated for by reversing the polarization period.

The pulse width of the idler pulse after second-stage amplification is 453 fs, as shown in Fig. S3**d**. The shortening of the idler pulse width is caused by the negative dispersion of the LN crystal at long wavelengths. Meanwhile, the asymmetry of the pulse envelope's leading and trailing edges is due to the idler pulse's overly broad spectral coverage, which results in different GDDs for different spectral components. However, as can be seen from the pulse-domain envelope, the nonlinear chirp modulation has little effect on our pulse-domain shape. This demonstrates that the idler pulses are compressible, providing an excellent seed source for subsequent 3 μm high-energy OPCPA systems.

We have designed and proposed a scheme for ultra-wideband infrared pulse quasi-phase-matched parametric amplification. Based on precise dispersion management and polarization period control, this scheme enables octave-spanning amplification of infrared pulses. Furthermore, using SSFM, we have theoretically calculated the specific details of this scheme and extended it to longer wavelengths and a broader spectral range. Based on the newly established OPA paradigm, this approach opens up new possibilities for the generation of high-power, ultra-broad-spectral-range light and its applications in coherent spectroscopy and attosecond science.